Mon. Not. R. Astron. Soc. **000**, 000–000 (2010) Printed 4 November 2010 (MN LATEX style file v2.2)

The GALEX Arecibo SDSS survey: III. Evidence for the Inside-Out Formation of Galactic Disks

Jing Wang[1,2⋆], Guinevere Kauffmann[2], Roderik Overzier[2], Barbara Catinella[2], David Schminovich[3], Timothy M. Heckman[4], Sean M. Moran[4], Martha P. Haynes[5] Riccardo Giovanelli[5], Xu Kong[1,6]

[1]*Center for Astrophysics, University of Science and Technology of China, 230026 Hefei, China*
[2]*Max–Planck–Institut für Astrophysik, Karl–Schwarzschild–Str. 1, D-85748 Garching, Germany*
[3]*Department of Astronomy, Columbia University, New York, NY 10027, USA*
[4]*Department of Physics and Astronomy, The Johns Hopkins University, Baltimore, MD 21218, USA*
[5]*Center for Radiophysics and Space Research, Cornell University, Ithaca, NY 14853, USA*
[6]*Key Laboratory for Research in Galaxies and Cosmology, University of Science and Technology of China, Chinese Academy of Sciences, China*

arXiv:1011.0829v1 [astro-ph.CO] 3 Nov 2010

Accepted by MNRAS; in original form 2010 September 01

ABSTRACT

We analyze a sample of galaxies with stellar masses greater than $10^{10}M_{\odot}$ and with redshifts in the range $0.025 < z < 0.05$ for which HI mass measurements are available from the GALEX Arecibo SDSS Survey (GASS) or from the Arecibo Legacy Fast ALFA survey (ALFALFA). At a given value of M_*, our sample consists primarily of galaxies that are more HI-rich than average. We constructed a series of three control samples for comparison with these HI-rich galaxies: one sample is matched in stellar mass and redshift (C_{M*}), the second sample is matched in stellar mass, $NUV-r$ colour and redshift ($C_{M*,NUV-r}$), and the third sample is matched in stellar mass, $NUV-r$ colour, stellar surface mass density μ_* and redshift. We generated self-consistent 7-band photometry (FUV, NUV, u, g, r, i, z) for all galaxies and we used this to derive inner colours, outer colours, asymmetry and smoothness parameters. We also used standard SED fitting techniques to derive inner and outer specific star formation rates. As expected, HI-rich galaxies differ strongly from galaxies of same stellar mass that are selected without regard to HI content. The majority of these differences are attributable to the fact that galaxies with more gas are bluer and more actively star-forming. In order to identify those galaxy properties that are *causally connected with HI content*, we compare results derived for the HI sample with those derived for galaxies matched in stellar mass, size and NUV-r colour. The only photometric property that is clearly attributable to increasing HI content, is the colour gradient of the galaxy. Galaxies with larger HI fractions have bluer, more actively star-forming outer disks compared to the inner part of the galaxy. HI-rich galaxies also have larger g-band radii compared to i-band radii. Our results are consistent with the "inside-out" picture of disk galaxy formation, which has commonly served as a basis for semi-analytic models of the formation of disks in the context of Cold Dark Matter cosmologies. The lack of any intrinsic connection between HI fraction and galaxy asymmetry suggests that gas is accreted smoothly onto the outer disk.

Key words: galaxies: evolution–ultraviolet: galaxies

1 INTRODUCTION

The fraction of the baryons in dark matter halos that are locked up in stars in the central galaxy reaches a maximum of 20%, at masses somewhat below that of the Milky Way, and falls rapidly at both higher and lower masses (Guo & White 2010). In the absence of feedback effects from supernova or AGN, most of these baryons are expected to cool, accrete and form stars (Kauffmann et al. 1993).

There is some observational evidence that gas from the external environment continues to accrete onto galaxies at the present day. Without a continuous supply of gas, most star forming galaxies would run out of gas on timescales of a few Gyr (Larson et al. 1980). HI cloud complexes, HI-rich dwarfs in the vicinity of spiral galaxies, extended and warped outer layers of HI in spiral galaxies, and lopsided galaxy disks have all been cited as evidence for ongo-

⋆ Email: wangj@mpa-garching.mpg.de

ing gas accretion in nearby galaxies (Sancisi et al. 2008). However, estimates of the accretion rates in the form of neutral hydrogen in nearby spirals consistently give values much lower than those required to sustain star formation at their observed rates (see Fraternali (2010) for a recent review). This leads to the hypothesis that most of the baryons that reside outside galaxies at the present are in the form of ionized gas (e.g. Fukugita, Hogan & Peebles 1998). There is also some evidence from observations of ionized silicon in high and intermediate-velocity clouds in the Milky Way, that gas in a low-metallicity ionized phase in the halo can provide a substantial (1 $M_\odot$/yr) cooling inflow to replenish star formation in the disk (Shull et al. 2009).

One interesting question that has not been considered very much in the literature, is whether gas accretes onto all galaxies in a smooth, continuous fashion, or whether accretion is more stochastic. If accretion has been stochastic, then galaxies that have recently acquired gas from the external environment might be expected to have unusually high HI mass fractions. The neutral gas content of a galaxy has long been known to correlate with its other physical properties. HI mass fractions increase smoothly along the Hubble sequence from the early-type (S0) to the late-type (Im) end (Roberts & Haynes 1994). There are also correlations between HI mass fraction and galaxy properties such as stellar mass (M_*), stellar mass surface density (μ_*) and broadband colour. These correlations form the basis for the so-called "photometric gas fraction" technique for predicting the HI gas content galaxies (Kannappan 2004; Zhang et al. 2009). Rather little attention has been given to the *scatter* in gas fraction at a given value of M_*, μ_* or colour. Recently, Zhang et al (2009) found that more gas-rich galaxies were systematically deficient in metals at fixed stellar mass and they interpreted this as evidence for recent cosmological infall of gas in these systems. However, up to now there has been no systematic study of how galaxy properties vary as a function of HI over- or under-abundance.

One problem that has hampered progress on this front has been the lack of suitable data sets. Blind HI surveys, such as the HI Parkes All Sky Survey (HIPASS, Barnes et al 2001) or the Arecibo Legacy Fast ALFA survey (ALFALFA, Giovanelli et al 2005) have produced large, unbiased samples of galaxies selected by HI mass. However, these surveys are still relatively shallow, so the fraction of HI-poor galaxies is small.

Recently, Catinella et al (2010, hereafter C10) explored how HI gas fraction scales as a function of galaxy stellar mass, galaxy structural parameters and NUV-r colour, using data from the GALEX Arecibo SDSS Survey (GASS). The survey is an ongoing large programme at the Arecibo radio telescope that is gathering high quality HI-line spectra for an unbiased sample of $\sim$ 1000 galaxies with stellar masses greater than $10^{10} M_\odot$ and redshifts in the range $0.025< z < 0.05$, selected from the Sloan Digital Sky Survey (SDSS, York et al. (2000)) spectroscopic and Galaxy Evolution Explorer (GALEX, Martin et al. (2005)) imaging surveys. The galaxies are observed until detected or until a low gas mass fraction limit (1.5-5 %) is reached. C10 quantify in detail how the *mean* atomic gas fraction of the galaxies in their sample decreases as a function of stellar mass, stellar mass surface density, galaxy bulge-to-disc ratio (as measured by the concentration index of the r-band light), and global NUV-r colour. The fraction of galaxies with significant (more than a few percent) HI decreases sharply above a characteristic stellar surface mass density of $10^{8.5}$ $M_\odot$ kpc^{-2}. The fraction of gas-rich galaxies decreases much more smoothly with stellar mass.

In this paper, we extend the study of C10 to study how the *resolved* UV/optical photometric properties of galaxies depend on atomic gas fraction. We have developed a photometric pipeline that transforms the SDSS and GALEX images to the same geometry and effective resolution, so that our photometric measurements trace the same part of each galaxy at different wavelengths (Wang et al 2009). We use these images to study UV-optical colours in their inner and outer regions of the galaxies in our sample and to study how colour (and hence specific star formation rate) *gradients* depend on HI content. In order to extend the range in M(HI)/M_* that we are able to probe, we combine the sample analyzed in C10 with galaxies from the GASS "parent sample" (described in Section 2) which have HI detections in the ALFALFA survey. This considerably improves the statistics for galaxies with large values of M(HI)/M_*, which are relatively rare. In order to isolate the effect of the presence or absence of gas on the photometric properties of galaxies, we compare our results with three control samples, which have similar optical properties to the galaxies in our sample with HI mass measurements, but are selected without regard to HI content. These control samples are described in detail in Section 2.3. Sections 3.1 and 3.3 present the methods used to measure our photometric parameters, and in Section 4 we discuss the trends in galaxy size, $NUV-r$ and specific star formation rate gradients, and higher order morphological parameters such as asymmetry and smoothness as a function of HI mass fraction. Finally Section 5 summarizes our results. Throughout this paper, we assume a cosmology with H_0=70 km s^{-1} Mpc^{-1}, Ω_m=0.3, and Ω_Λ=0.7 (Tegmark et al. 2004). A Chabrier initial mass function is assumed in the stellar population synthesis analysis (Chabrier 2003).

2 DATA

2.1 The parent sample

We select galaxies with stellar masses $M_* > 10^{10} M_\odot$ in the redshift range $0.025 < z < 0.05$ from the sixth data release (DR6) of the SDSS Survey, which lie within the maximal ALFALFA footprint. We match this catalogue with the fourth data release (GR4) of the GALEX survey and this yields a sample of 10468 galaxies. We further limit the sample to face-on galaxies with $b/a > 0.4$ (or an inclination of less than 66.4 deg) where b and a are the minor and major axes of an ellipsoidal fit (from SDSS r band) to each galaxy. This yields a final sample of 8429 galaxies, which we refer to as the *parent sample* from now on. We restrict the sample to face-on systems, so that our estimates of star formation rate, which are derived from the UV/optical photometry, will be less affected by dust attenuation effects (Section 3.3).

2.2 The sample of galaxies with HI mass measurements

This sample consists of galaxies in the parent sample for which we have catalogued HI detections from the 40% ALFALFA survey (α.40, which will be discussed in Martin et al. (2010) and Haynes et al. (2010)), as well as galaxies that are included in the first data release (DR1) of the GASS survey (see C10 for a detailed description). Our HI sample consists of 458 galaxies with a median HI mass fraction M(HI)/M$_*$ of $\sim$ 30%. Figure 1 shows the distribution of M(HI)/M$_*$ for these galaxies. The left-top panel of Figure 2 show a gallery of g, r, i colour images generated using the SDSS Image List Tool [1] for galaxies with stellar masses in the

[1] http://cas.sdss.org/astro/en/tools/chart/list.asp

range $10^{10.75}$ to $10^{11.5}$ $M_\odot$ and HI mass fractions (log M(HI)/M_*) in the range -0.84 to -0.48 dex. We note that the average value of log M(HI)/M_* for galaxies in this stellar mass range is ∼-1.4 (see C10), so these galaxies are all significantly more HI-rich than is typical.

2.3 Control samples

We limit the galaxy pool from which we draw the control galaxies to the regions of sky not yet covered by our current ALFALFA or GASS catalogues. The sample from which we draw the control galaxies comprises 5527 galaxies from the "parent sample". We create three control galaxy samples with similar optical properties to the galaxies with HI detections.

The first control sample (C_{M*}) is matched only in redshift and stellar mass. For each galaxy with an HI detection, we search within a distance of 0.028 dex in M_* and 0.005 in z for the nearest neighbor in the plane of stellar mass versus redshift. Each galaxy only enters the control sample once. We repeat this procedure twice, increasing the $\Delta \log M_*$ tolerance to 0.03 and 0.035, so that in the end, each galaxy with an HI-detection has 3 galaxies matched in stellar mass and redshift. The bottom-left panel of Figure 2 shows a montage of C_{M*} galaxies that have been matched to galaxies in Rows 1-2. Note that because the control galaxies are matched in redshift, we can meaningfully compare the morphologies, sizes and colours of the HI rich and corresponding C_{M*} galaxies in this figure.

Figure 3 compares the distributions of redshifts (z), stellar masses (log M_*), total $NUV - r$ colours, half-light radius (R_{50}), local environment densities [1] (ρ), concentration indices (R_{90}/R_{50}), $g - i$ colour difference ($\Delta(g-i)$, see Sect.3.1) and 25 mag arcsec^{-2} isophote diameters (D_{25}) for galaxies with HI measurements (open histograms) and for C_{M*} galaxies (hatched, red histograms). The logarithm of the KS-test probabilities that both histograms are drawn from the same underlying distribution are noted in the corner of each panel: a value of -2 means there is 99% confidence that the null hypothesis that the two samples are drawn from the same distribution can be rejected.

Figure 3 confirms the visual impression gained from comparing the left-top and left-bottom panels of Figures 2: Galaxies in our sample with measured HI masses are, on average, significantly more gas rich than C_{M*} galaxies and are also found to have bluer global colours, lower concentrations, larger sizes, and stronger negative colour differences (i.e. they are bluer on the outside). Galaxies with HI measurements are found in lower density environments, which is not too surprising, since galaxy colour and environment are known to be strongly correlated.

We have constructed a second control sample, $C_{M*,NUV-r}$, that is matched in $NUV - r$ colour in addition to stellar mass and redshift. For each galaxy with an HI measurement, we search within a distance of 0.18 dex in log M_*, 0.31 mag in $NUV - r$ colour and 0.005 in z for the nearest neighbor in the stellar mass-redshift-colour plane. Note that the chosen tolerances in log M_* and $NUV-r$ colour are comparable to the errors in these quantities. We repeat the above process again, with the log M_* distance increased to 0.25 and the ($NUV - r$) distance increased to 0.43 mag. In the end each HI galaxy has 2 control galaxies matched in stellar mass and ($NUV - r$) colour.

The $C_{M*,NUV-r}$ control sample (examples are shown in the right-top panel of Figure 2) allows us to investigate the extent to which the $NUV - r$ colour can serve as a "proxy" for the HI content of a galaxy. Note that this is the underlying assumption of many photometric gas fraction techniques – if HI fraction and colour are exactly equivalent, then the HI sample and the $C_{M*,NUV-r}$ control sample should have identical properties. Figure 4 presents histograms of the properties of these two samples. As can be seen, there is no longer any significant difference in concentration index between the sample with HI masses and the $C_{M*,NUV-r}$ control sample, but the size differences do persist. The differences in the distribution of local environment parameters and colour gradients decrease significantly, but are still significant.

Finally, we have constructed a third control sample, $C_{M*,NUV-r,\mu*}$, that is matched in half-light radius measured from the SDSS i-band image ($R_{50}(i)$) in addition to stellar mass, $NUV - r$ colour and redshift. For each galaxy with an HI measurement, we search within a distance of 0.3 dex in log M_*, 0.52 mag in $NUV - r$ colour, 1.9 kpc in $R_{50}(i)$, and 0.005 in z for the nearest neighbor in the stellar mass-redshift-colour-size plane. In this case, there is only one control galaxy matched to each HI galaxy. Catinella et al (2010) showed that a HI mass could be most accurately "predicted" using a linear combination of NUV$-r$ colour and $\log \mu_*$. Figure 5 shows that very few apparent differences between the HI sample and the the $C_{M*,NUV-r,\mu_*}$ control sample now remain. There is no longer any significant difference in the distributions of local environment parameters. There does appear to be a difference between the distribution of $g - i$ colour gradients, which we will investigate in more detail in the next section[2].

3 MEASUREMENTS

3.1 2-zone photometry

In this section, we analyze how the sizes and colour gradients of galaxies of fixed stellar mass depend on atomic gas fraction. We have generated two different sets of aperture-matched photometry for galaxies with HI measurements and also for the galaxies in our control samples. The first set of measurements is generated from GALEX FUV and NUV images, and SDSS images in the u, g, r, i and z-bands. Images in the FUV, u, g, r, i, and z bands are registered so that they have the same geometry as the NUV image, and are then convolved to the same effective resolution as the NUV image. All neighboring objects are masked and the r-band image is used as the reference for flux measurements in all other bands (see Wang et al. (2009) for details). We use this set of photometric measurements in our analysis of UV/optical colours and colour gradients, and for self-consistent SED fitting using all 7 photometric bands (FUV,NUV, u, g, r, i, z).

The second set of measurements is generated from the SDSS g and i band images, which have significantly higher resolution than the GALEX images (∼ 1 ″ instead of 5 ″). The i-band image is registered to match the geometry of the g band image, and the two images are convolved so that they match to a common PSF. The g-band image is used as the reference image for flux measurements in both bands. This set of photometric measurements is used whenever we consider only optical colours, sizes or colour gradients.

[1] Note that ρ is calculated as the number of tracer galaxies inside a cylinder of diameter 2 Mpc h^{-1} and length 16 Mpc h^{-1} divided by the mean number of galaxies inside such a cylinder at that redshift. The ρ values have been extracted from the NYU Value-Added Galaxy Catalog (Blanton et al. 2005)

[2] We also made a control sample similar to $C_{M*,NUV-r}$, but which excluded galaxies hosting active or composite nuclei (AGN) using the criteria in Kauffman et al. (2003). We did not find any difference in the results.

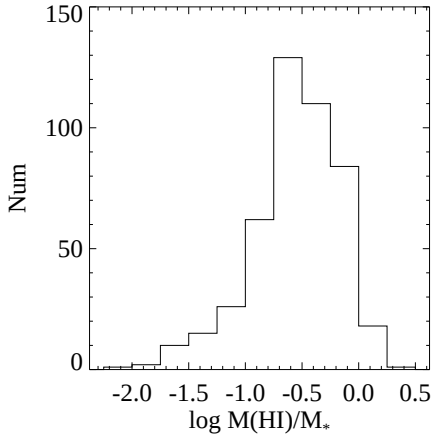

Figure 1. The distribution of HI mass fractions for the 458 galaxies in our sample with HI mass measurements.

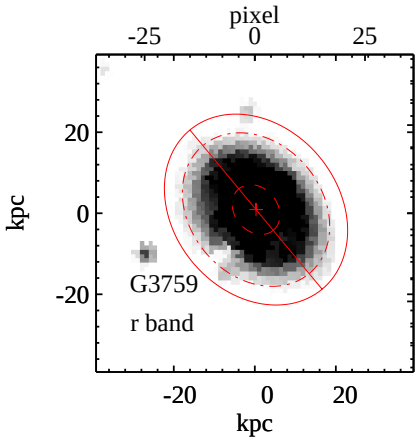

Figure 6. The convolved *r*-band image of the GASS galaxy G3759. The dashed line shows the half-light ellipse, the dashed-dotted line shows the 25 mag/arcsec^2 isophote, and the solid line shows the ellipse at 2.5 times the Kron radius. The region within the dashed line is defined to be the "inner" region, while the region between the dashed and the solid lines is defined as the "outer" region.

We divide each galaxy into an inner and an outer region: the former is enclosed by R_{50}, the radius enclosing half the total *r*-band light (determined from the PSF-convolved *r* band image), and the latter is defined as the region between R_{50} and 2.5 times the Kron radius (Kron (1980), also determined from the PSF-convolved *r* band image). We measure fluxes in all the bands for both regions. We define the $(NUV-r)$ colour difference $\Delta(NUV-r)$ as $(NUV-r)_{out}-(NUV-r)_{in}$ (likewise for $\Delta(g-i)$), so that negative values of Δ imply that the outer region of the galaxy is *bluer* than the inner region[3].

To illustrate, Figure 6 shows the HI-detected GASS galaxy G3759. The dashed curve indicates the ellipse enclosing half the *r*-band light, the dot-dashed curve indicates the 25 mag/arcsec^2 isophote, and the solid curve the ellipse with a semi-major axis equal to 2.5 times the Kron radius.

[3] We have checked that if we normalize the colour difference $\Delta(NUV-r)$ by the size of the galaxy, the results presented in this paper do not change.

3.2 Image stacking

In Appendix A, we demonstrate that the 2-zone $(NUV-r)$ color measurement is reliable only when the radius of the inner zone is larger than 6 arcsec (about the FWHM of the PSF of a GALEX NUV image) and the error on the total (NUV-*r*) colour ($\sigma(NUV-r)$) is smaller than 0.1 mag. If we were to apply both a size and an error cut, we would be left with $\sim$ 74% of the galaxies from the HI sample, $\sim$ 36% of the galaxies from the C_{M*} sample, $\sim$ 70% of the galaxies from the $C_{M*,NUV-r}$ sample and $\sim$ 74% of the galaxies from the $C_{M*,NUV-r,\mu*}$ sample. If we only apply the cut on size, 78% of the HI sample, 58% of the C_{M*} sample, 76% of the $C_{M*,NUV-r}$ sample and 80% of the $C_{M*,NUV-r,\mu*}$ sample remain.

One problem with making a cut in $\sigma(NUV-r)$ is that the remaining galaxies are biased toward NUV-bright (i.e. blue) objects, especially in the C_{M*} sample. In order to avoid this problem, we cut the sample only by size, and we stack the images in bins of stellar mass and HI gas fraction in order to boost the S/N of the colour measurements. We then measure average colour and SFR gradients for the stacked images. The increased S/N of the stacked images will also improve the quality of the SED fitting (Section 3.3).

We first select galaxies which have R_{50} larger than 6″, from the HI and "parent" samples. We then make new C_{M*}, $C_{M*,NUV-r}$ and $C_{M*,NUV-r,\mu*}$ control samples as described in Section 2.3. Because the "galaxy pool" from which we draw these control galaxies is now smaller, each galaxy from the HI sample only has one control galaxy matched in stellar mass and one control galaxy matched in stellar mass and $(NUV-r)$ colour. For simplicity, we will still call these three new samples the HI sample, C_{M*} sample, $C_{M*,NUV-r}$ sample and $C_{M*,NUV-r,\mu*}$ sample.

We divide the new HI sample into 4 stellar mass bins with log $M_*/M_\odot$ ranges of 10-10.25, 10.25-10.5, 10.5-10.75 and 10.75-11.5. Each stellar mass bin includes 80-90 galaxies. In each stellar mass bin, we further divide the galaxies into two groups at the median value of M(HI)/M_*. In total, the HI sample is divided into 8 groups for stacking, with 40-50 galaxies in each group. We also divide the matched C_{M*} and $C_{M*,NUV-r}$ samples into 8 groups for stacking; each group in these control samples will then be matched to the corresponding group from the HI sample.

Our stacking procedure consists of the following steps. We rescale the images to the median value of R_{50} for the galaxies in the group. We subtract the background, correct for Galactic extinction and any offset in photometric zeropoint, align the centers of all the

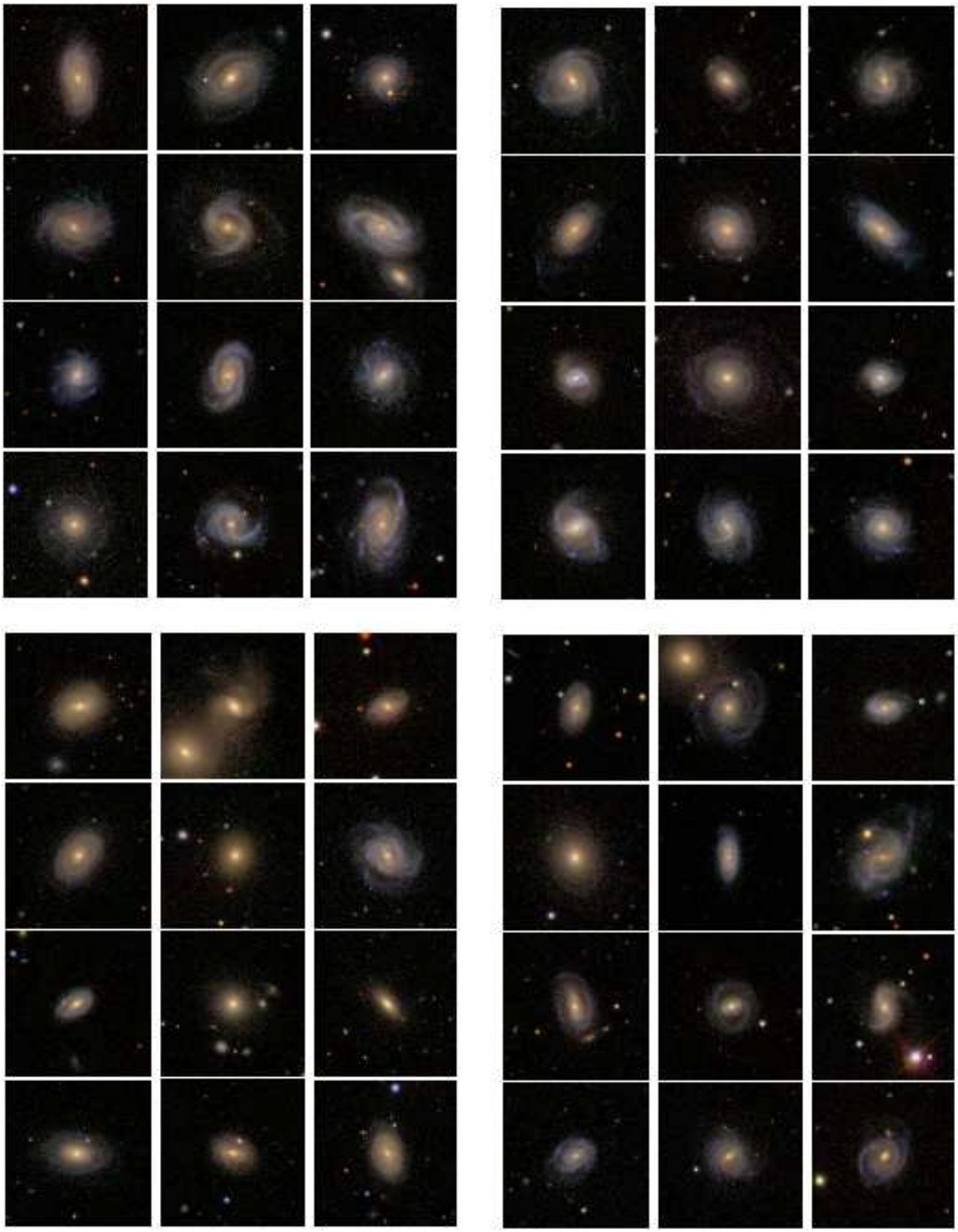

Figure 2. A montage of g, r, i colour images of galaxies selected from the HI sample (top-left panel), and the corresponding control galaxies from the C_{M*} (bottom-left panel), $C_{M*,NUV-r}$ (top-left panel) and $C_{M*,NUV-r,\mu_*}$ (bottom-right panel) samples. The scale of each image is ∼0.2″ pixel^{-1}. The galaxies are selected to have stellar masses in the range from $10^{10.75}$ to $10^{11.5}$ $M_\odot$. The galaxies from the HI sample are ordered by increasing $\log M(HI)/M_*$, from -0.84 to -0.48

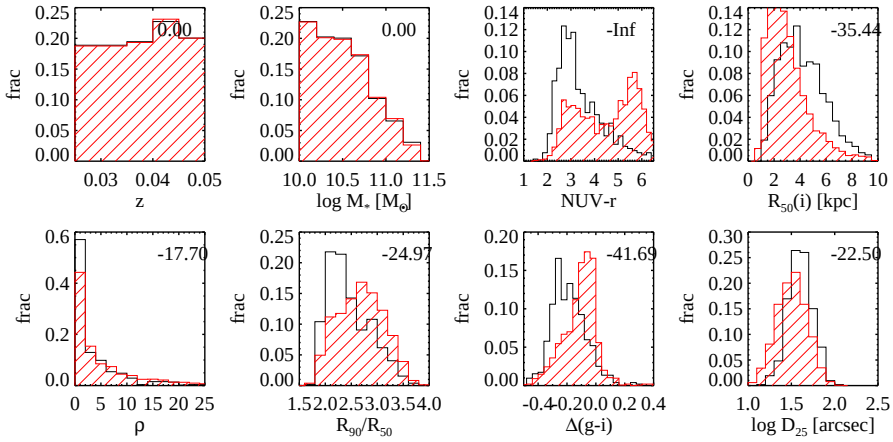

Figure 3. Comparison of distributions of redshifts (z), stellar masses (log M_*), total $NUV - r$ colours, half-light radii (R_{50}), local environment densities (ρ), concentration indices (R_{90}/R_{50}), $g - i$ colour differences ($\Delta(g - i)$) and 25 mag arcsec^{-2} isophote diameters (D_{25}) for the sample with HI measurements (open histograms) and the C_{M*} control sample (red, hatched histograms). The logarithm of KS-test probabilities that the two histograms are drawn from the same underlying distribution are denoted in the corner of each panel.

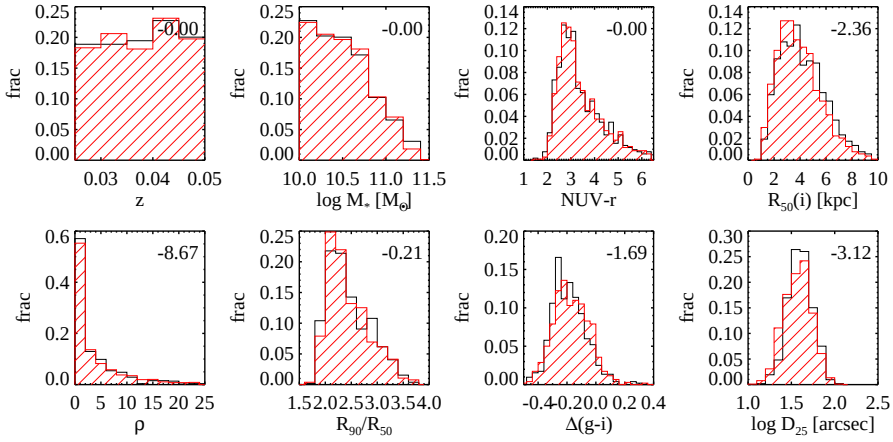

Figure 4. Same as Figure 3, but for the $C_{M*,NUV-r}$ control sample.

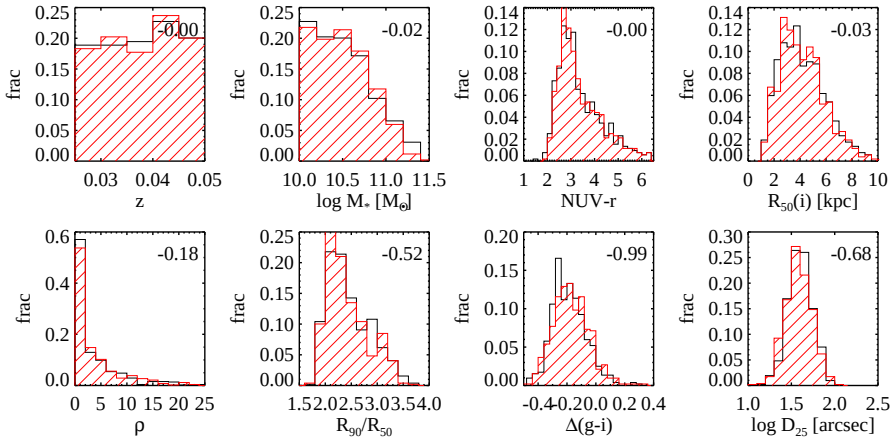

Figure 5. Same as Figure 3, but for the $C_{M*,NUV-r,\mu*}$ control sample.

images, and then add them together. We create stacked images for the images (convolved to the resolution of the NUV image) for all 7 photometric bands. The stacked *r*-band image is used as the reference image to measure photometric parameters. We note that the stacked images all have a $\sigma(NUV-r)$ less than 0.01.

3.3 2-zone specific star formation rates

We have used a spectral energy distribution (SED) fitting technique to derive the average specific star formation rates (sSFR) in the inner and outer regions of our stacked sample of galaxies. We follow the method from Salim et al. (2007), hereafter S07, with a few key changes that are detailed below. S07 used the Bruzual & Charlot (2003) population synthesis code to create a library of 100,000 model SEDs in 7 bands (FUV, NUV, $u, g, r, i, z,$) by generating model galaxies with a range of ages, star formation histories, metallicities and dust attenuation strengths. For a given galaxy, they evaluated the χ^2 goodness-of-fit by comparing the observed photometry with each model, determined the relative weight for each model, and finally built a probability distribution function (PDF) for the model parameters. The average of the PDF is adopted as the a nominal estimate of the parameters.

S07 show that the derived dust attenuation (the optical depth τ_V) is sensitive to the assumed prior distribution of τ_V in the model library, so the prior distribution should be as realistic as possible. To solve this problem, we estimate approximate values of the attenuation $\tau_V(gas)$ from the Balmer decrement F(Hα)/F(Hβ) within the SDSS fiber and the Calzetti et al. (2000) extinction curve, when both F(Hα) and F(Hβ) have $S/N > 3$. When either F(Hα) or F(Hβ) has $S/N < 3$, we adopt $\tau_V(star, fiber)/0.44$ from the measurements of the attenuation of the stellar continuum of the galaxy provided in the MPA/JHU catalog (*tauv_cont*). This parameter is obtained by fitting Bruzual & Charlot (2003) population synthesis models to the stellar continuum; the reddening may then be estimated by determining the extra "tilt" that must be applied to the models in order to fit the shape of the observed spectrum.

The prior distribution of $\tau_V(gas)$ and μ ($\tau_V(star) = \tau_V(gas) \times \mu$) values we adopt in our model library is tuned to reproduce the $\tau_V(star, fiber)$ predictions for the whole HI sample. We adopt for $\tau_V(gas)$ a Gaussian distribution peaked at 1.78, with a width $\sigma = 0.55$, and we adopt for μ a Gaussian ditribution peaked at 0.44 (Calzetti et al. 2000), with a width $\sigma = 0.4$. The Gaussian distribution for $\tau_V(gas)$ is trimmed so that it only spans values between 0 and 4, and the Gaussian distribution for μ is trimmed so that it only spans values between 0 and 1. Here we assume that the $\tau_V(star)$ does not change significantly throughout the galaxy.

In reality, the dust distribution in galaxies is more complicated than our simple model assumes. One issue is that for a typical galaxy, the relative attenuation between the inner disk, outer disk and bulge depends strongly on inclination (Tuffs et al. 2004). However, this effect becomes most notable when the inclination is large (axis ratio $b/a < 0.4$), so this problem is much mitigated by excluding galaxies with $b/a < 0.4$ from the samples (Section 2.1) (Yip et al. 2010). In the absence of more detailed information on the dust distribution in each galaxy, we believe our method gives results that are as accurate as possible.

To test the robustness of the sSFR derived from our SED fitting, we also measured sSFR directly from the SDSS fiber spectrum, and we compared this to the sSFR estimated within the 3 ″ aperture using our SED fitting technique. The SFR derived from the spectrum is calculated from the Hα luminosity, and corrected for dust using the Balmer decrement F(Hα)/F(Hβ) and the Calzetti et al. (2000) extinction curve. The stellar mass inside the SDSS fiber is taken from the MPA/JHU catalog. For SED fitting, we take the SDSS fluxes within the fiber from the SDSS archive (fibercounts), measure the GALEX NUV fluxes and convolved SDSS *u* band and GALEX FUV fluxes within 6 ″ around the galaxy (approximately the FWHM of the GALEX NUV PSF). Then we use the *u* band fluxes (within the fiber aperture and from the convolved images) to normalize the GALEX FUV and NUV fluxes, so that we get consistent SED from the 7 bands within the 3″ aperture.

We see from Figure 7 that the two estimates generally agree with each other, with a 1σ scatter of ∼0.39 dex. The offset between the two estimates exhibits weak systematic trends with both log SFR and τ_V. The most discrepant results are obtained for galaxies with very low specific star formation rates, where the UV luminosities are low and may trace populations of stars that are not properly accounted for in standard population synthesis models (Conroy & Gunn 2010). We have also tested the effect of varying the adopted priors for τ_V . We confirm that the prior that is most similar to the real distribution (as calculated from the spectrum), gives the best fit.

3.4 Morphological parameters

We closely follow the procedure described in Lotz et al. (2004), hereafter L04, to derive the asymmetry (*A*) and smoothness (*S*) parameters from the SDSS *g*-band images. Both *A* and *S* are measured inside an aperture equal to 1.5 times the petrosian radius (r_p). All neighboring objects are masked.

A is a measure of the difference between a given galaxy image and the image rotated by 180 degrees about the object center (the center is determined by minimizing *A*). A higher value of *A* means that the galaxy is more asymmetric. *S* is a measure of the difference between a given galaxy image and the image smoothed with a $0.2r_p$ wide boxcar kernel. A higher value of *S* implies that the galaxy has a more clumpy morphology on scales equal to the kernel size. *A* and *S* are also calculated using regions of blank sky in the vicinity of the galaxy; the average values of *A* and *S* calculated for the background are subtracted from the measurements we make for the galaxy.

To make sure that our measurements are consistent with L04, we measure *A* and *S* for 41 galaxies from L04 with images available from the SDSS. Our results are shown in Figure 8. We see that our parameters and those from L04 follow similar trends along the Hubble sequence. There is quite close agreement between the *A* values, but our *S* values are typically four times smaller than those of Lotz – this is likely to be a reflection of the different quality/resolution of the images or different details in the image processing steps in the two cases. Nevertheless, our test shows that the relative trends in *S* are the same for both sets of measurements, so these parameters are a useful diagnostic of relative changes in galaxy morphology.

We visually check all the images in our sample using the SDSS Imaging Finding Chart Tool [3], and we identify galaxies that are clearly undergoing a merger event. We find no enhancement in the merger fraction for the galaxies in the HI sample (9, 8, and 7 galaxies out of a total of 519 in the HI, C_{M*}, and $C_{M*,nuvr}$ samples exhibit clear signs of a merger or interaction in our images).

[3] http://cas.sdss.org/astro/en/tools/chart/chart.asp

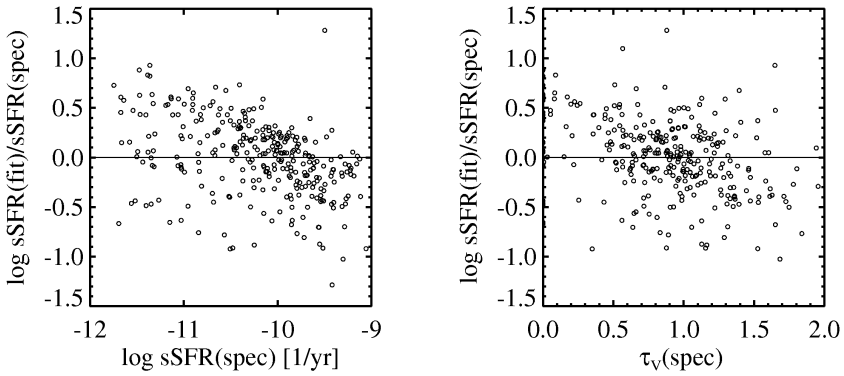

Figure 7. The difference between the sSFR derived from SED fitting and the sSFR measured from the dust-corrected Hα luminosity and stellar mass from the SDSS fiber spectrum. The difference is plotted as a function of sSFR (left) and $\tau_V(gas)$ within the fiber (right).

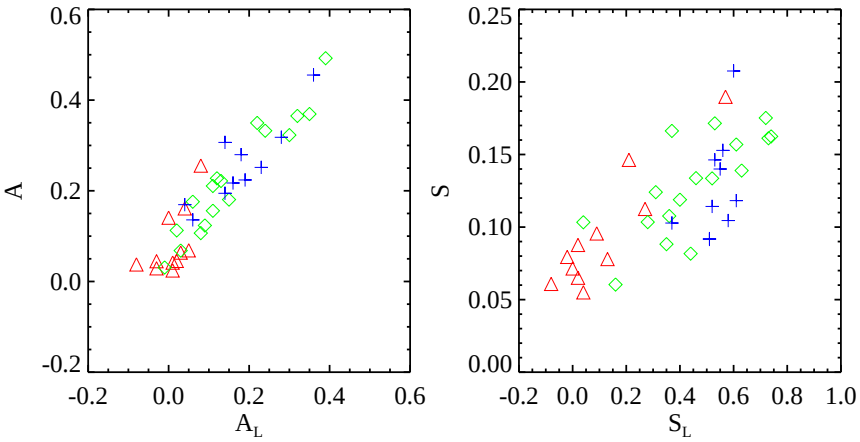

Figure 8. Comparison of morphological parameters measured by L04 (x-axis) and by us (y-axis). The red triangles are Sa galaxies, green diamonds are Sb galaxies and blue crosses are Sc galaxies.

4 RESULTS

As shown in Figures 2 and 3, galaxies from the HI sample are bluer, and have larger sizes and later type morphologies compared to C_{M*} galaxies. This is not surprising, because it is well known that galaxies that are more actively star-forming also contain more gas. The $C_{M*,NUV-r}$ and $C_{M*,NUV-r,\mu*}$ galaxies, on the other hand, are matched to the HI sample both in stellar mass and in global NUV-*r* colour, so if HI gas fraction and star formation activity track each other very closely, one might expect the galaxies in these two samples to have identical properties. In the following sections, we will show that this is not true. We divide the HI sample into four stellar mass bins, and study how sizes and colour gradients vary with atomic gas mass fraction. We also compare properties of the corresponding control galaxies along the same sequence. The main purpose of comparing our results with those derived from control samples is to isolate those trends that can be attributed to increasing HI content, rather than to any other correlated property, such as stellar mass or global star formation rate. Because the samples have all been matched in redshift, the noise in the measurements of luminosity and colour necessary to estimate quantities such as stellar mass, will be identical in all the comparison samples.

4.1 HI mass fraction and the optical sizes of galaxies

Figures 3 and 4 demonstrate that the galaxies in the HI sample have larger average sizes than both C_{M*} and $C_{M*,NUV-r}$ control sample galaxies. The mean value of $R_{50}(i)$ of the HI sample is larger by 1.2 and 0.3 kpc than the mean values of $R_{50}(i)$ of the C_{M*} and $C_{M*,NUV-r}$ control sample galaxies respectively. In Figure 9, we plot the relations between the half-light radius R_{50} and M(HI)/M$_*$ in four different bins of stellar mass for galaxies in the HI sample. The mean values of M(HI)/M$_*$ for each stellar mass bin are marked as crosses of different sizes at the bottom of the plot. These have been derived by Catinella et al (2010) using GASS survey galaxies for which HI masses have been measured down to a limiting M(HI)/M$_*$ limit of $\sim$ 1.5%. The majority of our HI-detected galaxies have atomic gas fractions that are above the average value – this is not surprising since galaxies detected in the ALFALFA survey make up the bulk of our sample.

We see that the half-light radius R$_{50}$ measured in the *g*-band increases as a function of M(HI)/M$_*$ at a given value of M_*. This result is consistent with the scaling relations published in Zhang et al (2009) and C10, which clearly showed that M(HI)/M$_*$ correlates strongly with stellar surface density μ_* (i.e. with galaxy size at a fixed value of the stellar mass). Indeed, both studies find that M(HI)/M$_*$ can be best predicted using a *combination* of colour and

μ_*. As discussed in Zhang et al (2009), these scalings can be understood in terms of the Kennicutt-Schmidt law of star formation (Kennicutt 1998), which states that the surface density of star formation scales with the surface density of cold gas as a power-law with slope $\sim$ 1.4. A star formation law of this form leads to the expectation that

$$\log M(HI)/M* = a \log \mu_* + b \log SFR/M_* + c, \quad (1)$$

where a, b and c are constants. The NUV-r colour is an excellent proxy for SFR/M_* (especially in the blue sequence), so this leads to a prediction of a linear relation linking HI mass fraction, NUV-r colour and stellar surface mass density. The two right hand panels of Figure 9 show that sizes of $C_{M*,NUV-r}$ and $C_{M_*,NUV-r,\mu_*}$ control galaxies exhibit the same increase as for the HI-detected galaxies. This supports our hypothesis that the scaling of galaxy size with HI mass fraction arises as a *consequence* of the star formation rate-gas surface density relation.

In Figure 10, we analyze trends in the ratio of the g-band and i-band half-light radii as a function of HI mass fraction. R50 defined in the g-band is always slightly larger than R50 defined in the i-band, because the light from younger stellar populations is generally spread over a larger effective radius than the light from older stellar populations. The ratio between the g and i-band radii increases as a function of gas fraction, and is also larger for more massive galaxies at a fixed value of M(HI)/M_*. As we will show in the next section, this difference in g- and i-band half-light radii is also found when we analyze $g-i$ colour gradients. In the panels to the right, we plot size differences for the three control samples. Neither the C_{M*} nor the $C_{M*,NUV-r}$ control samples show similar trends to the HI sample. The size differences do increase for more massive galaxies in the $C_{M*,NUV-r,\mu_*}$ control sample, but the effects are weaker than those observed for the sample with real HI mass measurements.

One might worry whether these trends arise because HI-rich galaxies are more dusty. We analyzed the correlation between optical depth τ_V and HI mass fraction, and find that τ_V does not increase with $M(HI)/M_*$. In addition, control galaxies matched in stellar mass and colour do not have smaller τ_V values than galaxies from the HI sample. We are thus led to the conclusion that there is an *intrinsic* correlation between M(HI)/M$_*$ and R50(g)/R50(i).

4.2 HI mass fraction and ($g-i$) colour gradients

In the top two panels of Figure 11, we analyze trends in the inner and outer $g-i$ colours of the galaxies in our four samples. In the bottom panel, we look at trends in ($g-i$) colour gradients. Our results are as follows:

Inner colours: The inner $g-i$ colour of a galaxy depends strongly on stellar mass, in the sense that more massive galaxies have redder inner colours. The inner $g-i$ colour depends only weakly on HI mass fraction at a given value of M_*. We see very similar trends in inner $g-i$ colour for control samples matched in $NUV-r$ colours. We conclude that the inner colour of a galaxy is primarily sensitive to its stellar mass.

Outer colours: The behaviour of outer $g-i$ colour as a function of stellar mass and HI fraction is very different to that of the inner colour. It depends strongly on HI mass fraction, in the sense that more HI-rich galaxies have bluer outer colours. At a fixed value of the HI mass fraction, there is no dependence on stellar mass. We see very similar trends in the $C_{M_*,NUV-r}$ and $C_{M_*,NUV-r,\mu_*}$ control samples, but not in the C_{M_*} control sample. This indicates that the outer colour of a galaxy is primarily sensitive to how much ongoing star formation there is in the galaxy.

Colour gradients: The $g-i$ colour gradient of a galaxy depends strongly on its HI mass fraction, in the sense that more HI-rich galaxies become bluer on the outside relative to the inside. At a fixed value of M(HI)/M$_*$, more massive galaxies have stronger colour gradients. None of the control samples exhibits exactly the same trends as the HI sample. In the $C_{M_*,NUV-r}$ and $C_{M_*,NUV-r,\mu_*}$ samples, the colour gradients for massive galaxies behave in much the same way as for the sample with HI measurements. For low mass galaxies, however, there is no trend in colour gradient with log M(HI)/M_* for the control galaxies. Our main conclusion, therefore, is that there is an intrinsic link between higher HI fractions and bluer outer disks.

4.3 HI mass fraction and gradients in ($NUV-r$) colour and sSFR

In this section we analyze trends in the inner and outer NUV-r colours and colour gradients as a function of HI mass fraction. The analysis is similar to that of the $g-i$ colours in the previous section, except that in this case, the average inner and outer colours are computed from stacked images due to the lower S/N of the NUV images. As we will show, the main advantage of studying NUV-r colours is the fact that the UV is a much more sensitive probe of the presence of young stars than the g-band, so that both the trends as a function of M_* and M(HI)/M_*, and the differences between the HI sample and the control samples found in the previous section are much enhanced.

The results shown in Figure 12 confirm essentially all the conclusions discussed in the previous section. The main qualitative difference we find by studying NUV-r colours rather than $g-i$ colours is that the behaviour of the colour gradients and the outer NUV-r colours as a function of HI mass fraction now differ more significantly from those exhibited by both the C$_{M*,NUV-r}$ and the C$_{M*,NUV-r,\mu_*}$ control galaxies. This strengthens our conclusion that the trend in the colour of the outer disk is fundamentally linked to the increase in the HI content of the galaxy.

We note that Figures 11 and 12 both show that it is the most massive galaxies with stellar masses $\sim 10^{11}$ M$_\odot$, and with relatively low HI gas fractions of $\sim$ 10%, that have the strongest colour gradients. Low mass galaxies have the highest HI gas fractions, but their colour gradients are relatively weak. It is interesting to investigate the morphology of the UV light for both kinds of systems. Figure 13 shows optical and NUV images for the 18 HI-sample galaxies with the most negative $\Delta_{o-i}(NUV-r) < -1.1$ as well as the 18 HI-sample galaxies which have the highest values of $M(HI)/M_*$ in the HI sample (we point out that, because the HI sample is stellar mass limited at 10^{10} M$_\odot$, we are missing a population with the highest HI mass fractions ($M(HI)/M_*$) at a fixed M(HI)). The galaxies with the most negative $\Delta_{o-i}(NUV-r)$ all have very red central regions and a blue outer disk. Many of them have bars, and the blue light tends to be located in a UV-bright ring around the bar (upper panels of Figure 13). Galaxies with the highest HI gas fractions are usually blue throughout the whole galaxy (lower panels of Figure 13).

Finally, Figure 14 shows plots equivalent to Figures 11 and 12 for the specific star formation rates we derive from fitting models to the UV through optical SEDs derived from the stacked images (see section 3.3). We caution that we have to make assumptions about the likely range of dust attenuation in our galaxy sample, as well as assumptions about how the dust might be distributed

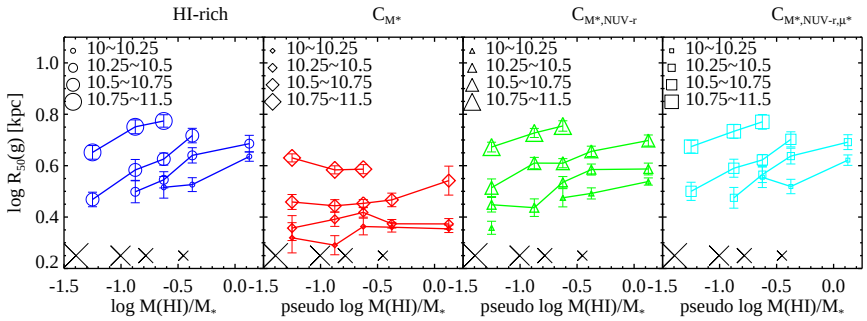

Figure 9. Relation between galaxy size (from the *g* band) and HI mass fraction for galaxies in the HI sample (blue circles), C_{M*} control sample (red diamonds), $C_{M*,NUV-r}$ control sample (green triangles) and $C_{M*,nuvr,\mu*}$ control sample (cyan squares). The control galaxies have no HI mass measurements, and are just plotted in the same M(HI)/M_* bin as the corresponding galaxies in the HI sample. Symbols of different sizes are for different stellar masses as indicated at the corners of the plots. The error bars show the r.m.s. deviation in the mean galaxy size calculated through bootstrapping. The crosses at the bottom of the plot mark the location of the mean gas fraction for galaxies in each stellar mass bin as given in C10.

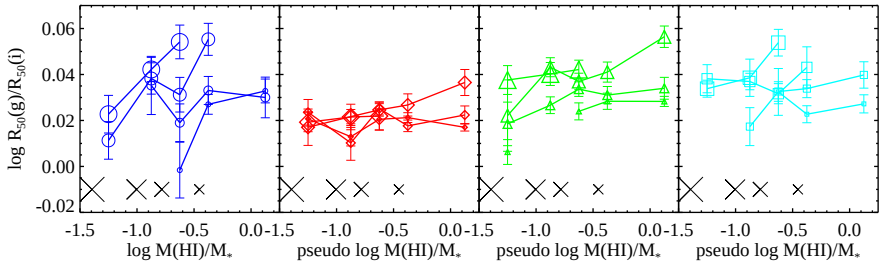

Figure 10. As in Figure 8, except for the ratio between the *g* and *i*-band half-light radii.

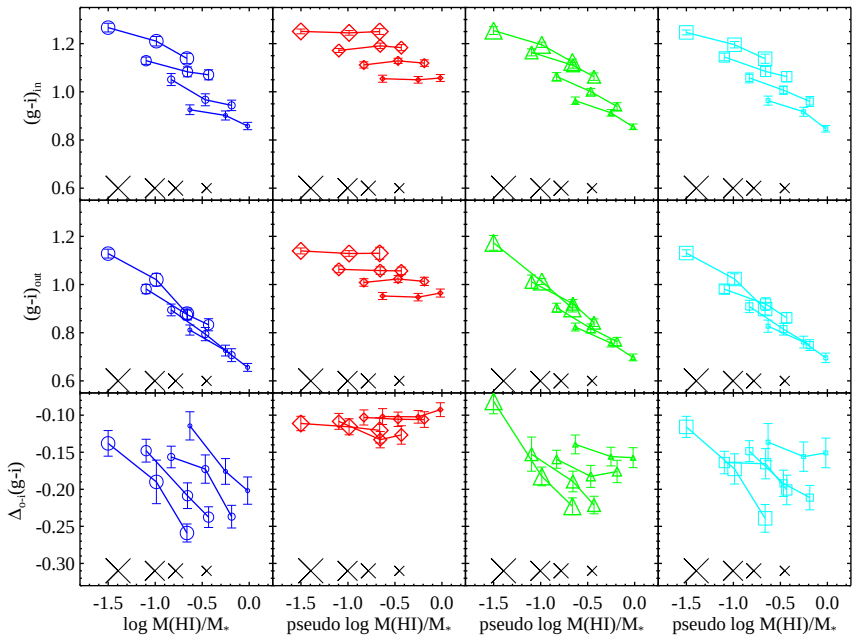

Figure 11. Relation between inner $g - i$ colour, outer $g - i$ colour and $\Delta_{o-i}(g - i)$ and HI mass fraction for the HI sample (left column, plotted as blue circles), C_{M*} control galaxies (second column, plotted as red diamonds) , the $C_{M*,NUV-r}$ control galaxies (third column, plotted as green triangles) and the $C_{M*,NUV-r,\mu*}$ control galaxies (fourth column, plotted as cyan squares). The control galaxies have no HI mass measurements, and are plotted in the same M(HI)/M_* bin as the corresponding galaxies in the HI sample. The sample is divided into 4 stellar mass bins, and plotted with symbols of different sizes as indicated in Figure 9. The error bars show the r.m.s. deviation in the mean values calculated through bootstrapping. The crosses denote the mean gas fraction for galaxies in each stellar mass bin (from C10).

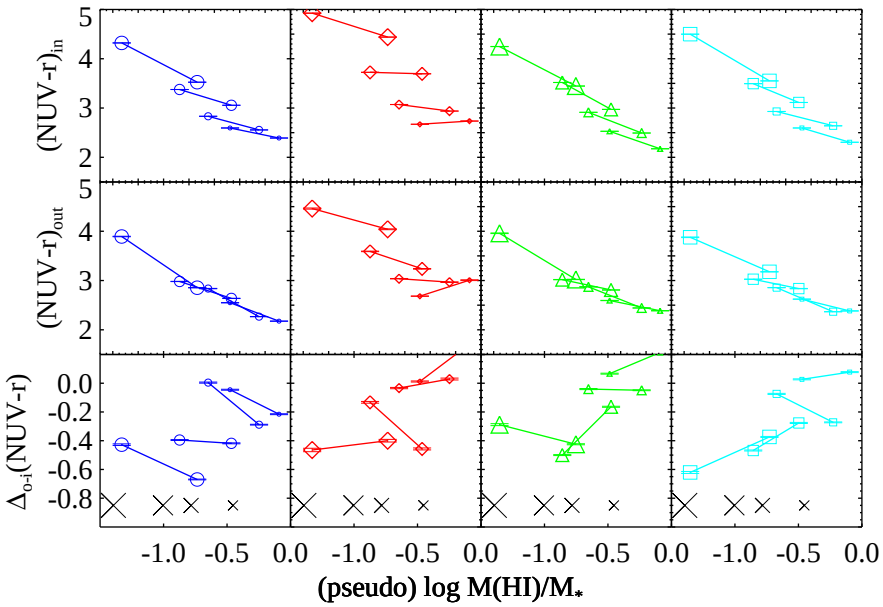

Figure 12. Relation between inner $NUV-r$, outer $NUV-r$, $\Delta_{o-i}(NUV-r)$ and HI mass fraction for the galaxies from the HI (blue circles) sample, and C_{M*} (red diamonds), $C_{M*,nuvr}$ (green triangles) and $C_{M*,nuvr,\mu*}$ (cyan squares) galaxies. The colours are measured from the stacked images. Note that the control galaxies have no HI mass measurements, and are plotted in the same M(HI)/M_* bin as the corresponding galaxies in the HI sample. Symbols of different sizes indicate different stellar masses as denoted in Figure 9 (larger symbol corresponds to higher stellar masses). The crosses denote the mean gas fraction for galaxies in each stellar mass bin (from C10).

throughout the galaxy. We thus regard these results as indicative, rather than definitive. The main point we wish to make with this plot is that with *plausible assumptions* about extinction, we find that outer disks are younger, with a higher ratio of present-to-past averaged star formation in galaxies with higher HI mass fractions. The same effect is not seen as clearly or strongly in the control samples. This implies that the outer disks of galaxies with higher HI mass fractions are are growing more rapidly, i.e. that these galaxies are forming from the "inside-out".

We have estimated the uncertainty in our estimated sSFR arising from the age-metallicity degeneracy. The offset between the estimated value of the sSFR will be less than 0.2 dex for galaxies with half-solar and twice solar metallicities. Note also, that all the galaxies in this analysis have $M_* > 10^{10} M_\odot$; the mass-metallicity relation (Gallazzi et al. 2005) implies that there will be no very low metallicity galaxies included in our analysis.

4.4 HI gas fraction and higher order morphological parameters

Figure 15 shows A and S as a function of HI fraction for the galaxies in the HI sample (blue), and for galaxies in the C_{M*} (red), $C_{M*,NUV-r}$ (green) and $C_{M*,NUV-r,\mu_*}$ (cyan) control samples. Galaxies in the HI sample are significantly more asymmetric and less smooth than galaxies in the C_{M*} sample. There is no significant difference between the HI, $C_{M*,NUV-r}$ and $C_{M*,NUV-r,\mu_*}$ samples. In Figure 16, we plot A and S as a function of HI mass fraction for galaxies in the HI sample (blue) and in the $C_{M*,NUV-r}$ control sample (green) for different stellar mass bins. We see that at fixed stellar mass, A and S both increase as a function of M(HI)/M_* for galaxies in the HI sample. At fixed stellar mass, galaxies in $C_{M*,NUV-r}$ sample have similar values of the asymetry parameter A and smoothness parameter S (except at the very highest HI mass fractions).

We conclude that the correlation of galaxy asymmetry and smoothness with HI mass fraction arises *because* galaxies with higher HI gas fractions have younger stellar populations. Reichard et al (2009) show that there is a strong link between galaxy asymmetry (in their case, as measured by the $m = 1$ azimuthal Fourier mode) and the age of its stellar population. They found that this link was independent of the other structural properties of the galaxy. Our analysis of the control samples appears to indicate that this link is also independent of HI content. Lopsidedness/asymmetry is believed to trace a non-equilibrium dynamical state caused by mergers, tidal interactions, asymmetric accretion of gas, or asymmetries related to the dark matter halo (Bournard et al. 2005). As discussed in section 3.4, we found no enhancement in the fraction of galaxies undergoing mergers in the HI sample relative to control samples, so it is perhaps not too surprising that we find no intrinsic correlation between lopsidedness/asymmetry and HI content.

5 DISCUSSION AND CONCLUSIONS

We have analyzed a sample of galaxies from the *parent sample* of the GASS survey, for which HI mass measurements are available from the GASS survey itself and from ALFALFA. At a given value of M_*, our sample consists primarily of galaxies with larger-than-average values of M(HI)/M_* . We use a combination of optical photometry from the SDSS and FUV,NUV images from GALEX to study properties of the 2-zone stellar populations of these HI-rich systems, and we investigate how they vary with HI mass fraction.

We constructed three control samples for comparison with the galaxies with HI mass measurements: one sample is matched in stellar mass and redshift (C_{M*}), the second one is matched in stellar mass, $NUV-r$ colour and redshift ($C_{M*,NUV-r}$) and the third one is matched in stellar mass, $NUV-r$ colour, surface mass density and redshift ($C_{M*,NUV-r}$). We then generated self-consistent 7-band

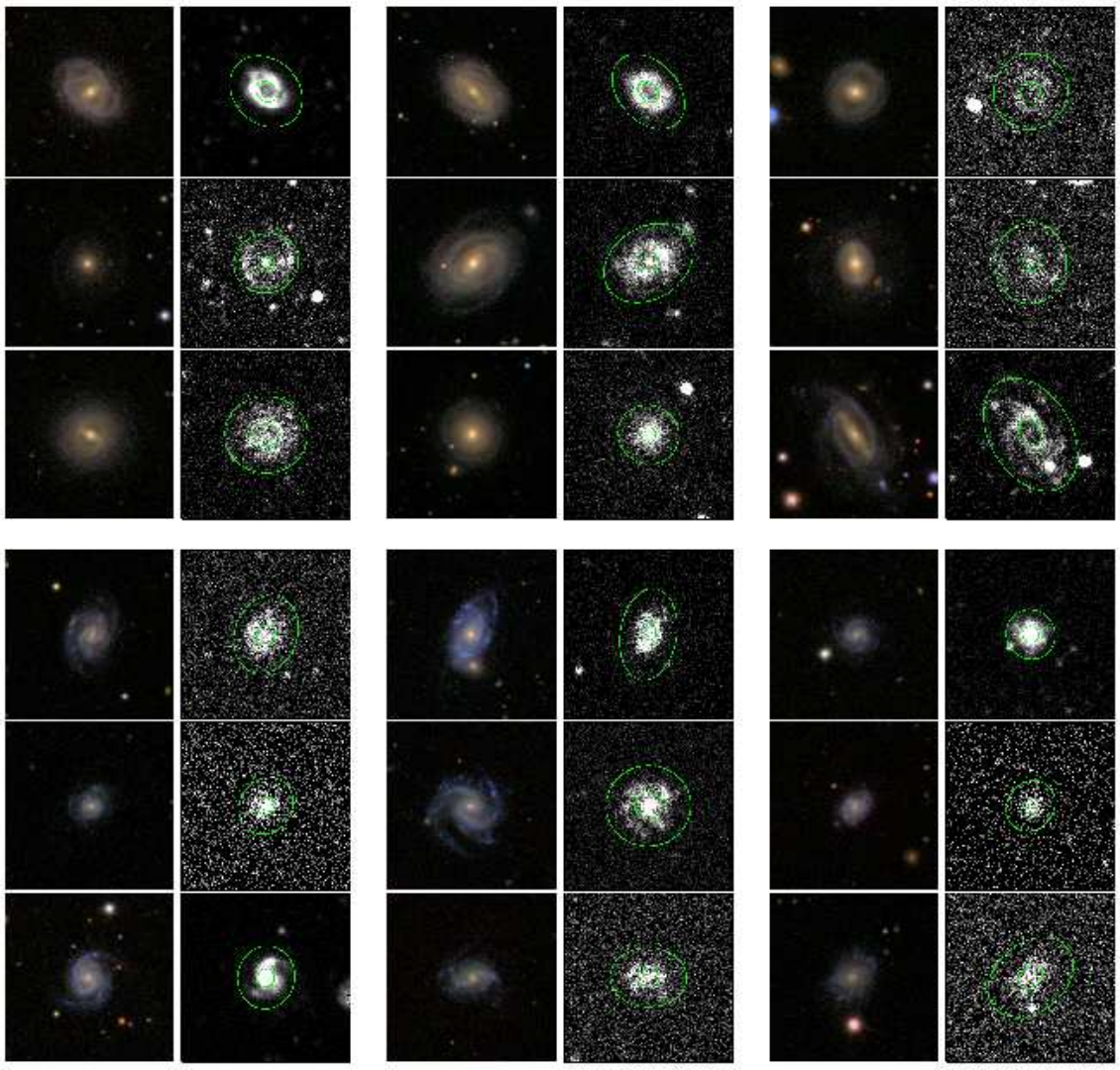

Figure 13. SDSS and GALEX NUV images of galaxies from the HI sample which have the most negative $(NUV-r)$ colour differences ($\Delta_{o-i}(NUV-r)$¡-1.1) (the first 3 rows), and of galaxies that have the highest HI mass fractions (M(HI)/M_*) ($\sim$ 1) (last 3 rows). For each image pair, the left image is the SDSS g, r, i colour composite image, and the right image is the NUV map for the same galaxy.

photometry (FUV, NUV, *u*,*g*,*r*,*i* and *z*) for the galaxies in all three samples and derived inner colours, outer colours, asymmetry and smoothness parameters for all the galaxies. We also generated four sets of stacked images in different bins of stellar mass and HI gas fraction, and used these to derive inner and outer specific star formation rates using an SED-fitting technique.

The main purpose of comparing our results with those derived from control samples is to isolate those trends that can be attributed to increasing HI content, rather than to any other correlated property, such as stellar mass or global star formation rate. As expected, HI-rich galaxies differ in nearly all their properties from galaxies of the same stellar mass selected without regard to HI content. Most of these differences are attributable to the fact that galaxies with more gas are bluer and more actively star-forming. In order to identify those galaxy properties that are *truly causally connected with HI content*, we also compare our results derived for the HI sample with those derived for galaxies with the same distribution of both stellar mass *and* NUV-*r* colour. Finally, Catinella et al (2010) have demonstrated that the best *predictor* of the HI gas fraction is a linear combination of NUV-*r* colour and the logarithm of the stellar surface mass density of the galaxy. At a fixed colour, galaxies with lower stellar mass densities have higher HI gas fractions. This motivates comparison with a control sample that is matched in stellar mass, NUV-*r* colour *and* stellar surface mass density.

We find that the only photometric property that is clearly attributable to increasing HI content and not to the total amount of star formation in the galaxy, is the *colour gradient* of the galaxy. There appears to be a causal link between HI fraction and outer disks that are bluer with respect to the inner part of the galaxy. The same effect also manifests itself as a systematic increase in the ratio of size of the galaxy measured from SDSS images in the *g*-band to that measured in the *i*-band. The colour gradients are significantly stronger if one analyzes UV/optical colours than if one uses $g-i$ as a tracer. Our SED modelling demonstrates that as the HI fractions of galaxies increase, the specific star formation rates in their outer regions become higher with respect to their inner regions. This means that the outer regions of HI-rich galaxies are *younger*.

Control samples that are matched in size in addition to colour

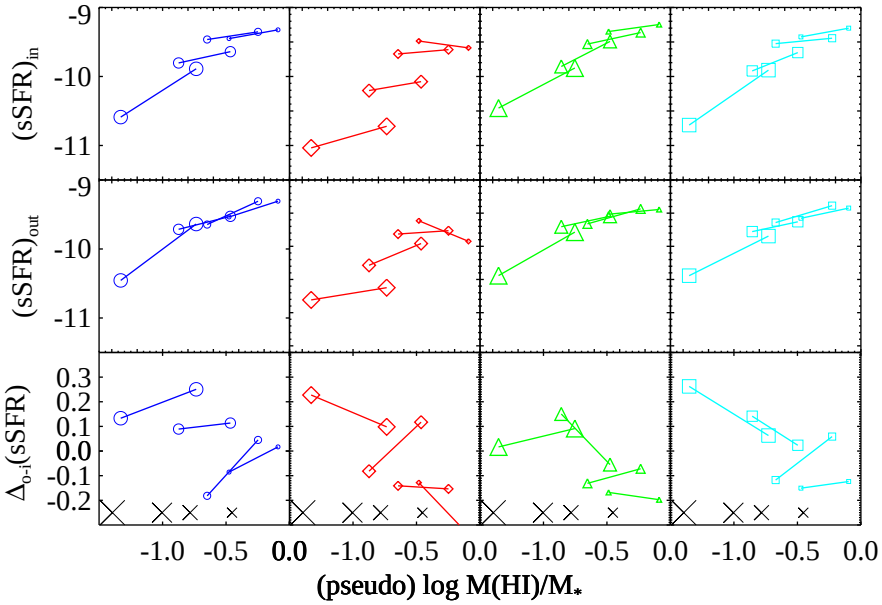

Figure 14. Relation between inner $sSFR$, outer $sSFR$, $\Delta_{o-i}(sSFR)$ and HI mass fraction for galaxies from the HI (blue circles) sample, and from the C_{M*} (red diamonds), $C_{M*,nuvr}$ (green triangles) and $C_{M*,nuvr,\mu*}$ (cyan squares) control samples. The sSFR are derived from SED fitting as explained in the text, and the SEDs are measured from the stacked images. Note that the control galaxies have no HI mass measurements, and are plotted in the same M(HI)/M$_*$ bin as the corresponding galaxies in the HI sample. Symbols of different sizes indicate different stellar masses as denoted in Figure 9 (larger symbol corresponds to higher stellar masses). The crosses denote the mean gas fraction for galaxies in each stellar mass bin (from C10).

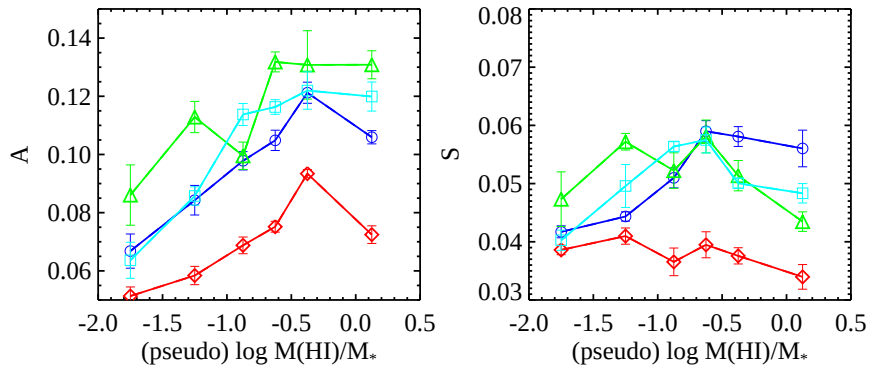

Figure 15. Relation between the median values of the morphological parameters asymmetry (A) and smoothness (S) and HI mass fraction for galaxies in the HI sample (blue symbols and lines). The median A and S values of the corresponding C_{M*} galaxies are plotted in red; results for $C_{M*,NUV-r}$ galaxies are shown in green; results for $C_{M*,NUV-r,\mu*}$ galaxies are shown in cyan. A median value is plotted only when there are more than 6 galaxies in that bin. Error bars show the r.m.s. deviation calculated through bootstrapping.

and stellar mass, tend to exhibit stronger colour gradients, but the observed scalings are still weaker than for the sample with real HI mass measurements. This indicates that colour gradients and size are partially co-variant, as might be expected if infalling gas was recently added to the outside of the disk in the most HI-rich galaxies in our sample.

The "inside-out" picture of disk galaxy formation has commonly served as a basis for semi-analytic modelling the chemical evolution of disk galaxies (e.g. Chiappini et al. 1997), as well as the formation of disk galaxies in the context of Cold Dark Matter cosmologies (e.g. Kauffmann 1996; Van den Bosch 1998; Boissier & Prantzos 1999; Dutton 2009). In this scheme, gas in the halo surrounding the galaxy cools, falls onto the galaxy while conserving its angular momentum, and fuels star formation in the disk. Gas accreted at late time has higher specific angular momentum, and so settles in the outer region of the galaxy. However, hydrodynamical simulations of the formation of disk galaxies indicate that angular momentum is not conserved and disks do not always form from the inside out (Sommer-Larsen et al 2003; Robertson et al 2004).

Direct observational evidence that disk galaxies form from the inside out has thus far been quite difficult to establish. Pohlen & Trujillo (2006) found that 60% of local disk galaxies have inner exponential profiles followed by a steeper (downward bending) outer exponential profile, while 30% have a shallower (upward bending) outer profiles. Azzollini et al (2008) find that for a given stellar mass, the radial position of this break has increased with cosmic time by a factor of 1.3+/-0.1 between $z = 1$ and 0, in agreement with a moderate inside-out growth of disk galaxies over the last ~ 8

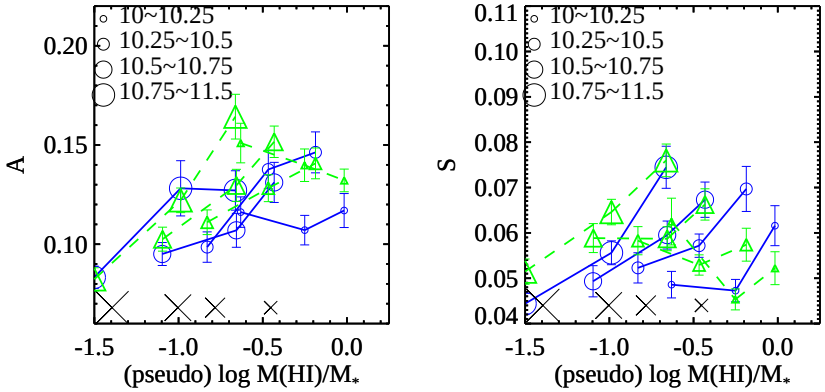

Figure 16. Relation between A and S and HI mass fraction for galaxies from the HI (blue circles) sample and from the $C_{M*,NUV-r}$ (green triangles) control sample. The sample is divided into 4 stellar mass bins, indicated by symbols of different sizes as described in the corner of each panel. The error bars show the r.m.s. deviations in the mean values of A and S calculated through bootstrapping. The crosses denote the mean gas fraction for galaxies in each stellar mass bin (from C10).

Gyr. Cresci et al (2009) find evidence for evolution in the zero point of the Tully-Fisher relation of galaxy disks at $z \sim 2$ with respect to local samples that is in agreement with cosmological simulations of disk galaxy formation.

Coherent studies of the metallicity, colour and star formation rate gradients in local galaxies have been few and far between. Zaritsky, Kennicutt & Huchra (1994) performed a careful study of abundance gradients derived from HII regions in a sample of 53 nearby spiral galaxies. They found that the slopes of the radial abundance gradients when rescaled to units of dex/isophotal radius, do not correlate with the luminosity or Hubble type of the galaxy. They did find evidence that galaxies with bars have flatter abundance gradients, which suggests that gas inflows may be important in understanding the time evolution of metallicity gradients. de Jong (1996) investigated the effects of star formation history and the metallicity on the colour profiles of 86 face-on spiral galaxies, and found that the outer regions of disks are on average younger and of lower metallicity. Munoz-Mateos et al (2007) studied specific star formation rate profiles of a sample of 160 nearby spiral galaxies from the GALEX Atlas of Nearby galaxies (Gil de Paz et al. 2007). They found a large dispersion in the slope of the sSFR profiles, with a slightly positive mean value, which they interpreted as implying moderate net inside-out disk formation. They found that in a minority of galaxies, the scale length of the UV light is significantly larger than the scale length of the near-IR light, and interpreted these galaxies as having undergone an episode of enhanced recent growth.

In this paper we have uncovered a direct link between the HI content of a galaxy and its specific star formation rate profile. This lends further credence to the idea that galaxies where the outer disk is very blue and actively star-forming compared to the inner disk have recently accreted gas. The fact that there is no intrinsic correlation between the HI fraction and the measured asymmetry of the optical light of the galaxy, suggests that the gas was accreted smoothly and not in discrete units. What is still lacking, however, is clear proof that the gas in HI-rich galaxies has been added to the outer disk recently. It will also be extremely important to obtain data that will allow us to *link* the cold gas content, specific star formation rates and metallicity gradients of disk galaxies in a self-consistent way. Only then, may we hope to fully constrain models of disk galaxy formation and chemical evolution.

We are currently engaged in an observational program to obtain accurate and homogeneous molecular gas masses for a subset of 300 galaxies from the GASS sample (Saintonge et al, in preparation; see http://www.mpa-garching.mpg.de/COLD_GASS/). In addition, we are obtaining long-slit spectra for the same galaxies using the MMT telescope (the 6.5m MMT telescope on Mt. Hopkins, AZ). Early results indicate that specific star formation rate and metallicity gradients in HI-rich galaxies are indeed tightly correlated (Moran et al. 2010). We intend to quantify this in more detail with larger samples of galaxies in our future work.

ACKNOWLEDGEMENTS

We thank Y. M. Chen, L. Wang, D. Christlein, G. W. Fang, C. Li, H. Guo and H. L. Yan for help with identifying bars. This will be the subject of a future paper. We thank L. Shao, C. Li, Y. M. Chen and S. White for useful discussions. XK is supported by the National Natural Science Foundation of China (NSFC, Nos. 10633020, and 10873012), the Knowledge Innovation Program of the Chinese Academy of Sciences (No. KJCX2-YW-T05), and National Basic Research Program of China (973 Program; No. 2007CB815404).

GALEX (Galaxy Evolution Explorer) is a NASA Small Explorer, launched in April 2003, developed in cooperation with the Centre National d'Etudes Spatiales of France and the Korean Ministry of Science and Technology.

We thank the many members of the ALFALFA team who have contributed to the acquisition and processing of the ALFALFA dataset over the last six years. RG and MPH are supported by NSF grant AST-0607007 and by a grant from the Brinson Foundation.

Funding for the SDSS and SDSS-II has been provided by the Alfred P. Sloan Foundation, the Participating Institutions, the National Science Foundation, the U.S. Department of Energy, the National Aeronautics and Space Administration, the Japanese Monbukagakusho, the Max Planck Society, and the Higher Education Funding Council for England. The SDSS Web Site is http://www.sdss.org/.

REFERENCES

Azzollini R., Trujillo I., Beckman J. E., 2008, ApJ, 684, 1026

Barnes D. G., et al., 2001, MNRAS, 322, 486
Blanton, M. R., Schlegel, D. J., Strauss, M. A., Brinkmann, J., Finkbeiner, D., et al., 2005, AJ, 129, 2562
Boissier, S., Prantzos, N., 1999, MNRAS, 307, 857
Bournard, F., Combes, F., Jog, C.J. & Puerari, I. 2005, A&A, 438, 507
Bruzual, G. & Charlot, S., 2003, MNRAS, 344, 1000
Calzetti, D., Armus, L., Bohlin, R. C., Kinney, A. L., Koornneef, J., Storchi-Bergmann, T., 2000, ApJ, 533, 682
Catinella, B., Schiminovich, D., Kauffmann, G., Fabello, S., Wang, J. et al., 2010, MNRAS, 403, 683 (C10)
Chabrier, G., 2003, PASP, 115,763
Chiappini C., Matteucci F., Gratton R., 1997, ApJ, 477, 765
Conroy C., Gunn J. E., 2010, ApJ, 712, 833
Cresci G., et al., 2009, ApJ, 697, 115
De Jong, R.S., 1996, A&A, 313,377
Dutton A. A., 2009, MNRAS, 396, 121
Fraternali F., 2010, arXiv, arXiv:1001.3879
Fukugita M., Hogan C. J., Peebles P. J. E., 1998, ApJ, 503, 518
Gallazzi, A., Charlot, S., Brinchmann, J., White, S. D. M., Tremonti, C. A., 2005, MNRAS, 362, 41
Gil de Paz, A., Boissier, S., Madore, B. F., Seibert, M., Joe, Y. H., 2007, ApJS, 173, 185
Giovanelli, R. et al. 2005, AJ, 130, 2598
Governato, F., Willman, B., Mayer, L., Brooks, A., Stinson, G., et al., 2007, MNRAS, 374, 1479
Guo Q., White S., Li C., Boylan-Kolchin M., 2010, MNRAS, 404, 1111
Haynes et al. 2010, in prep
Kannappan, S. J., 2004, ApJ, 611, 89
Kannappan, S. J., Guie, J. M., &Baker, A. J., 2009, AJ, 138, 579
Kauffmann G., 1996, MNRAS, 281, 475
Kauffmann, G., Heckman, T. M., Tremonti, C., Brinchmann, J., Charlot, S. et al. 2003, MNRAS, 346, 1055
Kauffmann, G., White, S. D. M., Guiderdoni, B., 1993, MNRAS, 264,201
Kennicutt, R. C., 1998,, ARA&A, 36, 189
Kron, R.G., 1980, ApJS, 43, 305
Larson, R. B., Tinsley, B. M., &Caldwell, C. N., 1980, ApJ, 237, 692
Lotz, J. M., Primack, J., Madau, P., 2004, AJ, 128, 163 (L04)
Martin, D. C. et al. 2005, ApJ, 619, L1
Martin, A. M., Papastergis, E., Giovanelli, R., Haynes, M. P., Springob, C. M. &Stierwalt, S. 2010, ApJ, in press, (arXiv:1008.5107)
Moran, S. M., Kauffmann, G., Heckman, T. M., Gracia-Carpio, J., Saintonge, A., et al. 2010, ApJ, 720, 1126
Muñoz-Mateos, J. C, Gil de Paz, A., Boissier, S., Zamorano, J., Jarrett, T. et al. 2007, ApJ, 658, 1006
Pohlen M., Trujillo I., 2006, A&A, 454, 759
Roberts, M. S., Haynes, M. P., 1994, ARA&A, 32, 115
Robertson B., Yoshida N., Springel V., Hernquist L., 2004, ApJ, 606, 32
Salim, S., Rich, R. M., Charlot, S., Brinchmann, J., Johnson, B. D., Schiminovich, D., 2007, ApJS, 173, 267 (S07)
Sancisi, R., Fraternali, F., Oosterloo, T., van der Hulst, T., 2008, A&A Rev., 15, 189S
Shull J. M., Jones J. R., Danforth C. W., Collins J. A., 2009, ApJ, 699, 754
Sommer-Larsen J., Götz M., Portinari L., 2003, ApJ, 596, 47
Tegmark, M., Strauss, M.A., Blanton, M.R. et al., 2004, Phys. Rev. D, 69, 103501
Trujillo, L., Pohlen, M., 2005, ApJ, 630, 17
Tuffs, R. J., Popescu, C. C., Völk, H. J., Kylafis, N. D., Dopita, M. A., 2004, A&A, 419, 821
van den Bosch F. C., 1998, ApJ, 507, 601
Wang, J., Overzier, R., Kauffmann, G., von der Linden, A., Kong, X., 2009, MNRAS, 401, 433
Xilouris, E. M., Byun, Y. I., Kylafis, N. D., Paleologou, E. V., Papamastorakis, J., 1999, A&A, 344, 868
Yip, C., Szalay, A. S., Wyse, R. F. G., Dobos, L., Budavári, T., Csabai, I., 2010, ApJ, 709, 780
York, D. G. et al. 2000, AJ, 120, 1579
Zaritsky, D., Kennicutt, R. C., Huchra, J. P., 1994, ApJ, 420, 87
Zhang, W., Li, C., Kauffmann, G., Zou, H., Catinella, B., et al., 2009, MNRAS, 397, 1243

APPENDIX A: A TEST OF THE ROBUSTNESS OF OUR 2-ZONE UV/OPTICAL COLOUR MEASUREMENTS

In this paper, UV/optical colours are measured by convolving the SDSS images to match the poorer resolution of the GALEX NUV images. In some of our galaxies, the half-light semi-minor axis b_{50} becomes similar to or smaller than the size of the $\sim$ 4 pixel PSF of the GALEX NUV images. In this regime, the 2-zone colour and SFR measurements may no longer be valid. In addition, the GALEX MIS images are relatively shallow, so the 2-zone measurements of the NUV fluxes may have large errors if the signal-to-noise is low.

In order to quantify these effects more precisely, we have performed simulations by transforming the images of nearby galaxies so that they have similar magnitudes and apparent size ranges to the galaxies in the samples studied in this paper. We select 52 galaxies from the GALEX Nearby Galaxies Survey (NGS, Gil de Paz et al. (2007)) with images available from the SDSS. We only select isolated galaxies with apparent sizes (D_{25}) less than 5 arcmin, where the image is not contaminated by foreground or background objects.

We begin by measuring $NUV - r$ and $\Delta_{o-i}(NUV - r)$ from these images (shown in purple in Figure A3). The nearby sample turns out to have a similar distribution of these two parameters as the GASS *parent sample* (shown in black on in Figure A3).

We then create a library of 60,000 simulated images. For each nearby galaxy image, we select a value of b_{50} and r-band apparent magnitude at random from the distributions shown in black in Figure A3. We also select a NUV image exposure time at random, again based on the real distribution of exposure times for the GASS parent sample. The NUV and r band fluxes are always rescaled so that the total $NUV - r$ colour is conserved. After rebinning in size, the NUV and r band images are convolved with the GALEX and SDSS PSFs and background and poisson noise are added. Figures A1 and A2 show two examples of the resulting simulated images. Figure A1 shows a typical galaxy, which is blue on the outside (with negative $\Delta_{o-i}(NUV-r)$), while Figure A2 shows a galaxy that is blue on the inside (with positive $\Delta_{o-i}(NUV - r)$).

After creating our library of 60,000 simulated images, we measure photometric parameters following the same steps described in Section 3.1. The distribution of output NUV-r colours, r-band apparent magnitudes, semi-minor axis size (b_{50}) and NUV-r colour gradient values are plotted as red histograms in Figure A3. We can see that the output values do differ from the input values.

To quantify this in more detail, the left panel of Figure A4

shows how the difference between output and input colour gradients change as a function of b_{50}, for galaxies with high S/N UV images ($\sigma(NUV-r) < 0.1$). When $b_{50} > 4$ pixels (which corresponds to 6 $''$), the output $\Delta_{o-i}(NUV-r)$ is quite close to the input value (systematically high by ∼0.05 mag on average). The scatter in the recovered gradient is less than 0.2 mag. When $b_{50} < 4$ pixels, the mean value of $diff(\Delta_{o-i}(NUV-r))$ rises steeply and the scatter in the recovered value also increases. We thus impose a lower limit on b_{50} of 4 pixels when we analyze UV/optical photometry in this paper (see Sect. 3.2).

The right panel of figure A4 shows the difference between the output and input colour gradients as a function of the errors on the $NUV-r$ colour, for galaxies with $b_{50} > 4$ pixels. The average offset remains constant at ∼0.05 mag when $-\log\sigma(NUV-r) > 0.5$, and then rises steeply towards lower values of $-\log\sigma(NUV-r)$. However, when $-\log\sigma(NUV-r) < 1$ (or $\sigma(NUV-r) > 0.1$), the scatter in the recovered gradient is already about 0.2 mag. This is because the outer UV light has lower surface brightness than the inner light. We conclude that $\sigma(NUV-r) < 0.1$ mag should be adopted as a lower S/N limit for robustly measuring total and 2-zone NUV-r colours.

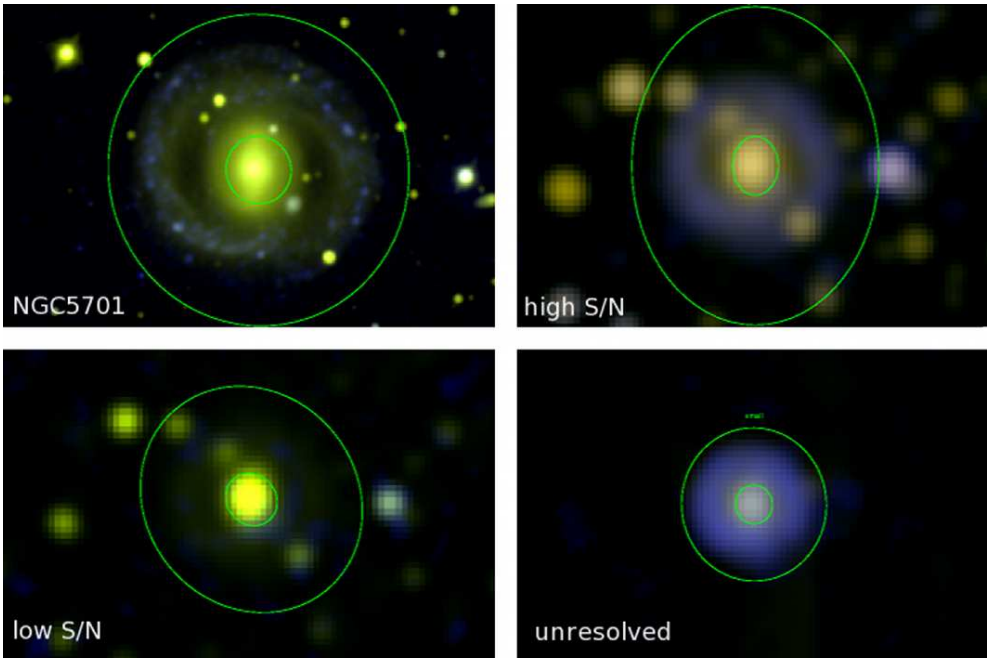

Figure A1. Original and simulated images of the galaxy NGC 5701. The left-top panel shows the original image, the top-right panel shows a simulated image with high S/N, the bottom-left panel shows a simulated image with low S/N, and the bottom-right panel shows an unresolved simulated image with high S/N. The two ellipses on each galaxy image mark the inner and outer regions of the galaxy.

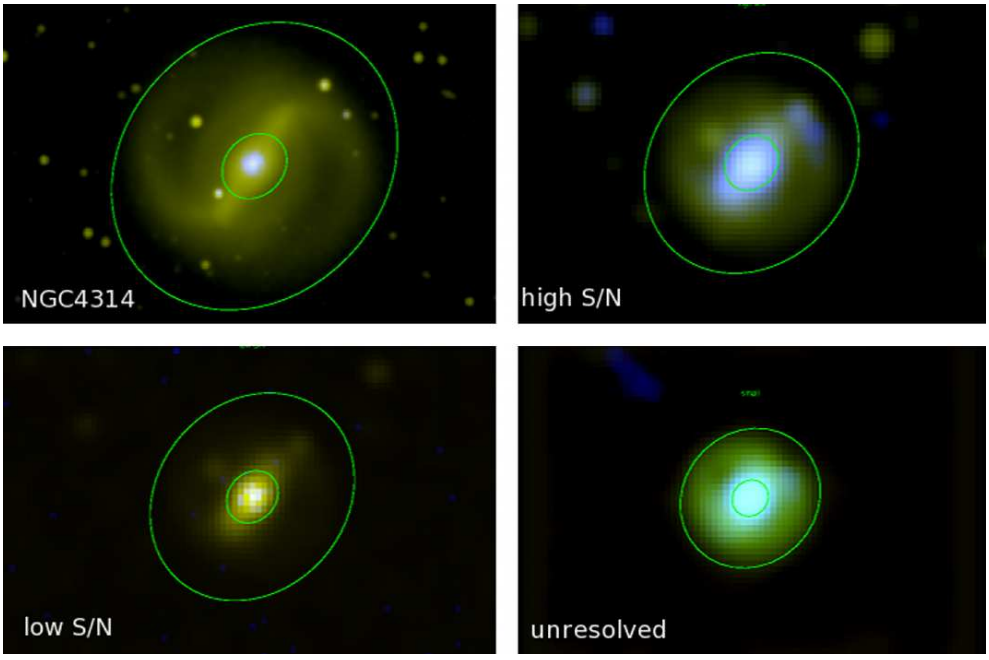

Figure A2. As in the previous figure, except for galaxy NGC 4314, which has a blue core.

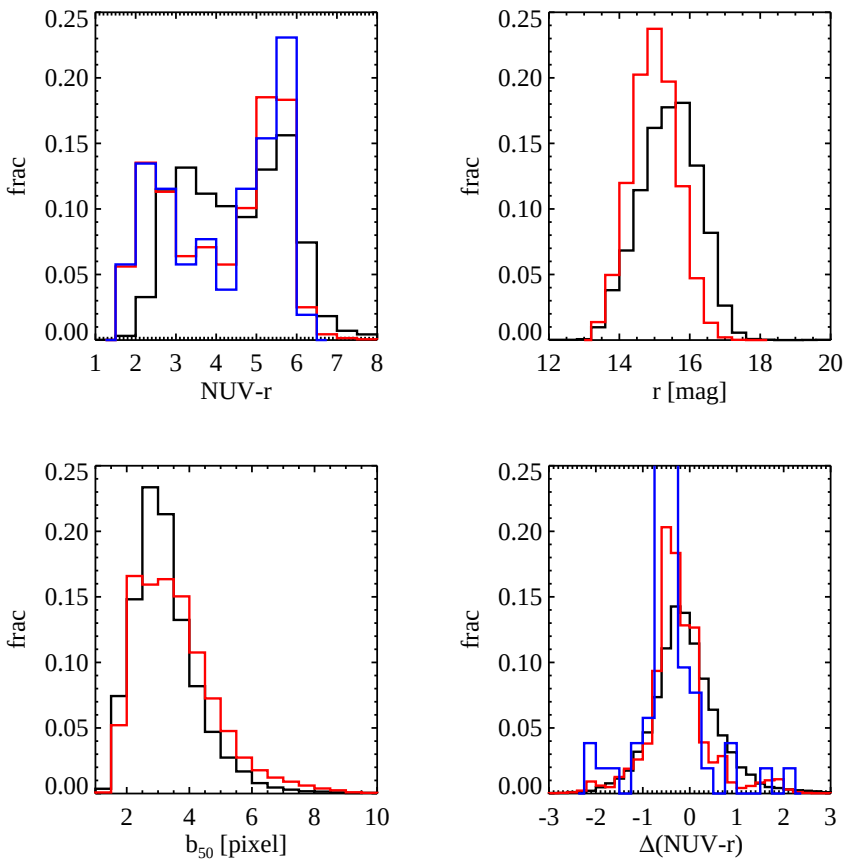

Figure A3. Distributions of $NUV - r$ colours, r band apparent magnitudes, semi-minor axis radii (b_{50}) measured in the r-band, and colour differences ($\Delta_{o-i}(NUV - r)$) for the GASS parent sample (black), for the original NGS galaxies (blue), and for the simulated images (red).

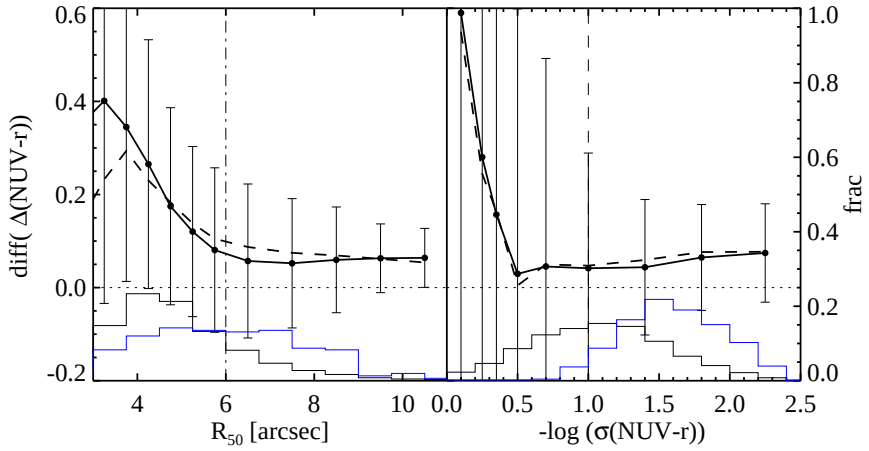

Figure A4. The average difference between the $\Delta_{o-i}(NUV - r)$ colour for the simulated galaxy images and the original galaxy images is plotted as a function of half-light radius of the galaxy in arcsec (left), for cases where $\sigma(NUV - r) < 0.1$. In the right panel, the average difference is plotted as a function of $NUV - r$ colour errors, for cases where $b_{50} > 4$ pixels. The solid lines show the average difference in each b_{50} bin, the dashed line shows the median, and the error bars show the r.m.s. scatter in the difference around its mean value. The dotted lines mark where the offset equals 0, and the dot-dashed lines mark the location of our recommended size and error thresholds discussed in Sect. 3.2.